Magnetic skyrmion diode: Unidirectional skyrmion motion via symmetry breaking of potential energy barriers

Dae-Han Jung, Hee-Sung Han, Namkyu Kim, Ganghwi Kim, Suyeong Jeong, Sooseok Lee, Myeonghwan Kang, Mi-Young Im, and Ki-Suk Lee

Magnetic Skyrmion Diode: Unidirectional Skyrmion Motion via Symmetry Breaking of Potential Energy Barriers

Dae-Han Jung[1], Hee-Sung Han[1,2], Namkyu Kim[1], Ganghwi Kim[1], Suyeong Jeong[1], Sooseok Lee[1], Myeonghwan Kang[1], Mi-Young Im[2] and Ki-Suk Lee[1*]

[1]Depearment of Materials Science and Engineering, Ulsan National Institute of Science Technology, Ulsan 44919, Republic of Korea

[2]Center for X-ray Optics, Lawrence Berkeley National Laboratory, Berkeley, CA 94720, USA

We realize a magnetic skyrmion diode operated by a unidirectional skyrmion transport that flows in only one direction, which is highly significant for information processing in spintronic and nanoelectronic devices. We facilely control the skyrmion transport by engineering asymmetric shapes of geometric structures. Here, we present a simple method to describe the underlying mechanism behind the unidirectional skyrmion transport, by characterizing the topography of potential energy surfaces from a purely geometric perspective. Our approach enables a deeper physical insight into skyrmion transport manipulation and efficient design of skyrmion-based devices in geometric structures.

Electrical diodes, operated by a unidirectional current flux, are elementary building blocks of contemporary computation, communications, and sensing [1,2], which have facilitated dramatic innovations in fundamental science and applied technology in various aspects of our daily lives. Inspired by the unidirectional effect of electrical diodes, significant interest has been devoted to the study of the unidirectional propagation of transport phenomena in a range of physical branches, such as microfluidics [3–6], heat-transfer dynamics [7,8], acoustics [9–12], photonics [13,14], and magnetism [15-18]. Analogous unidirectional transport is also suitable for application to magnetic skyrmions, which are regarded as promising information carriers due to their particle-like nature with topological stability, high mobility, and small size [19–29]. Indeed, it has been well established that skyrmions can be stable carriers of topological charge (Q) as they are topologically protected by the quantization of their topological charge [30,31] in the nonlinear σ model [32] in the form of chiral spin textures with the Dzyaloshinskii–Moriya interaction (DMI) [33,34].

Owing to this topological charge, skyrmions have unique dynamical properties referred to as the skyrmion Hall effect, analogous to the Magnus and Hall effects, which causes the skyrmions to acquire transverse velocity components to an external driving force [35,36]. Hence, within boundaries of a confined structure, the transport of skyrmions flows selectively on one side; if the direction of the external driving force is inverted, it flows on the other side. The mobility of the skyrmion transport is crucially affected by pinning sites such as geometric defects or

constrictions that hinder the movement of skyrmions [37–40].

Considering the skyrmion Hall effect and the pinning effect, we found a unidirectional skyrmion transport in which the skyrmion flows asymmetrically on two sides of a nanostrip edge such that the transport on one side is trapped by a pinning site but escapes from the pinning site on the other side. This was achieved by asymmetrically distributing pinning sites between the two sides such that one side possesses a pinning site but the opposite side does not. In this model, we numerically demonstrated a skyrmion diode that allows skyrmion transport from one end (input) to the other (output) but inhibits transport in the opposite direction of the driving force. However, there are counterintuitive phenomena in this unidirectional skyrmion transport; i.e., skyrmion transport is permitted on the side with a pinning site but prohibited on the side without a pinning site. Moreover, it is too costly and tedious to evaluate the criterion for the pinning–depinning of skyrmion transport by solving the skyrmion equation of motion, known as Thiele's equation [41], because it requires the state data of the nonlinear skyrmion dynamics for every time step.

In this work, we unambiguously reveal the underlying mechanism behind unidirectional skyrmion transport and its counterintuitive pinning phenomena, based on a simple description through characterizing the topography of potential energy (PE) surfaces from a purely geometric perspective. Our approach allows us to theoretically find the criterion for the pinning–depinning of skyrmion transport and efficiently design a skyrmion diode that can be applied to a wide variety of systems.

We perform micromagnetic numerical simulations [42] to display the impacts of pinning sites in forming an energy barrier to block skyrmion transport, and its unidirectional effect. To insert a pinning site asymmetrically on two sides of a nanostrip edge, a round-shaped pinning site is patterned on the top side (see Fig. 1), whereas the bottom side is not patterned. A periodic boundary condition along the longitudinal direction of the nanostrip is implemented to consider the effect of the asymmetric edge boundary on the two sides of finite width. Nanostrip dimensions of a cross-sectional area of 60×0.6 nm^2 and a pinning site depth of 20 nm are selected. In this nanostrip, a Néel-type magnetic skyrmion is initially located at $\mathbf{R}_0 = (x_0, y_0) = (\pm 274, 0)$ nm on either the left or right side relative to the pinning-site center. We can generate a skyrmion at $\mathbf{R}_0$ as proposed in various ways [51-54]. The skyrmion is driven to move toward the pinning site by applying in-plane dc currents in opposite ($\pm x$) directions. For simplification, we assume that the current density J_e is spatially homogeneously distributed throughout the nanostrip. Under application of the in-plane current J_e with various values of the damping constant α and nonadiabaticity β, the skyrmion is transported toward one of the two sides of the nanostrip edge by the Hall-like behavior of skyrmion motion. As the skyrmion approaches the nanostrip edge, the PE increases to repel the skyrmion from the boundary, serving as a confining potential. This confining PE is the total magnetic energy represented in the x–y plane of the skyrmion's center position $\mathbf{R} = (x, y)$, which mainly results from locally tilted magnetizations near the edge boundary [26,50,55–57]. Figure 1(a) shows the spatial distribution of the confining PE, $W_{con}(\mathbf{R})$,

4

in both pseudocolor plane and surface form. The skyrmion is annihilated within a certain distance from the boundary [57,58], depicted by the black area in the pseudocolor plane. The energy surface of $W_{con}(\mathbf{R})$ exhibits a locally formed energy ridge under the influence of the geometry of the pinning site. The skyrmion travels in this confining PE $W_{con}(\mathbf{R})$, and its current-driven trajectories for time-varying displacement $\mathbf{R}(t) = [x(t), y(t)]$ are shown in Figs. 1(b) and 1(c). The observed dynamic behaviors are distinct regarding the direction of electron flow: the skyrmion driven in the forward direction by the $-x$-directional current with density $J_e = +5$ MA/cm^2 [positive and negative signs of J_e denote the electron flowing in the forward ($+x$) and backward ($-x$) directions, respectively] passes through the pinning site, whereas the skyrmion driven by the current in the opposite (reverse) direction with $J_e = -5$ MA/cm^2 is pinned at the pinning site. In our model, the energy ridge of W_{con} plays the important role of an energy barrier separating the two distinct dynamic states (*on/off* states) of the skyrmion transport.

To theoretically elucidate and explain the concept of our model, we introduce the ansatz [41] for translational motion of a skyrmion $\mathbf{m} = \mathbf{m}[\mathbf{r} - \mathbf{R}(t)]$ where $\mathbf{m}$ is the unit vector of magnetization $\mathbf{m}(\mathbf{r}) = \mathbf{M}(\mathbf{r})/M_s$ with saturation magnetization M_s, which parametrizes its center of mass $\mathbf{R}$ in the x–y plane instead of $\mathbf{r}$. For steady-state motion $\mathbf{R}(t) = \mathbf{v}t$, the velocity can be obtained from Thiele's equation [41,59,60], expressing the balance of gyrotropic, dissipative, confining, and spin-transfer forces:

$$\mathbf{G} \times \dot{\mathbf{R}} + \widehat{D}\dot{\mathbf{R}} + \mathbf{F}_{\text{con}}(\mathbf{R}) + \mathbf{F}_{\text{STT}}(\mathbf{R}) = 0, \qquad (1)$$

where the gyrocoupling vector $\mathbf{G} = G\hat{\mathbf{z}}$ is proportional to the skyrmion number $Q = (1/4\pi) \int \mathrm{d}x\mathrm{d}y\, \mathbf{m} \cdot (\partial_x \mathbf{m} \times \partial_y \mathbf{m}) = 1$, such as $G = \mu_0(4\pi Q)M_s d/\gamma$ with film thickness d; $\widehat{D}$ is the dissipative tensor [61]; $\mathbf{F}_{\text{con}} = -\nabla_{\mathbf{R}} W_{\text{con}}$ is the confining force from the boundary edge; and $\mathbf{F}_{\text{STT}}$ is the spin-transfer torque (STT) force. For a continuous and irrotational STT field occupied in a simply connected region, we can imaginarily assign an effective PE for the STT on the $\mathbf{R}$-space, although it is not derived from an actual magnetic energy density. Here, the STT-PE (W_{STT}) is given by $W_{\text{STT}} = \int \mathbf{F}_{\text{STT}} \cdot \mathrm{d}\mathbf{R}$ with the gradients $-\partial_x W_{\text{STT}} = \widehat{D} \cdot \beta u$ and $-\partial_y W_{\text{STT}} = G \cdot u$ [61–63], where $u = J_e \mu_B P/eM_s$ is the effective spin-current drift velocity [57], μ_B is the Bohr magneton, e is the electronic charge, and P is the degree of spin polarization [46-48]. This W_{STT} is an additional energy to ascend the energy ridge (energy barrier), provided through its tilted energy plane.

By solving the equation of motion (1) for $\mathbf{R}$, the trajectory of a skyrmion can be obtained as the skyrmion displacement $\mathbf{R}(t) = [x(t), y(t)]$ travels a sequential temporal evolution of a kinematic state $(x, y, \dot{x}, \dot{y})$ from an initial state. The temporal characteristics provide an exact solution for the trajectory, but a lengthy time to find a criterion is redundant for determining *on/off* states. However, the possible paths that the skyrmion may take can be time-independently identified through an equipotential line in a conservative system, in which the STT-driven

skyrmion moves along the equipotential line $W_{tot} = W_{con} + W_{STT} = $ const. from a given initial

energy state $W_{tot}(\mathbf{R}_0, J_e)$. Assuming $\widehat{D}\dot{\mathbf{R}} \sim 0$, this approach is applicable to our model for the

following reasons: (1) The gyrotropic response of the skyrmion to a confining PE is conservative.

The adiabatic term of STT is also a conservative quantity for the adiabatic process of skyrmion

motion. (2) The nonadiabatic term of STT in this model is conservative because the spatially

homogeneous u makes the STT pseudofield $(-\beta(u \cdot \nabla)\mathbf{m}/|\gamma|)$ a scalar field that is curl-free and

simply connected [64,65]. If the divergent magnetization configuration of the Néel skyrmion

causes the curl of the pseudofield to be nullified, a spatially inhomogeneous u could also cause

the nonadiabatic term acting on a Néel skyrmion to be conservative.

Based on this approach using equipotential lines, the comparison between $W_{tot}(\mathbf{R}_0, J_e)$

and a critical energy value W_{tot}^* can significantly simplify the determination of *on/off* states at

the pinning site. The critical energy value W_{tot}^* can be easily obtained if we consider the

topography of two PEs: the local region of $W_{con}(\mathbf{R})$ near the pinning site is a saddle surface with

a negative Gaussian curvature (see Fig. S1), whereas the other region of $W_{con}(\mathbf{R})$ is a convex

energy surface with a positive curvature; the energy plane $W_{STT}(\mathbf{R})$ has zero curvature

everywhere on the $\mathbf{R}$-space. Here, the critical energy value W_{tot}^* corresponds to a saddle point

located on the energy ridge. In general, the saddle point can be found by evaluation of the

eigenvalues and corresponding eigenvectors of the Jacobian and Hessian [66–68]. For example,

if the eigenvalue of the Jacobian is zero and the Hessian is indefinite at a given point, then that

point is a saddle point. However, the Jacobian and Hessian for numerically obtained $W_{tot}(\mathbf{R})$ are sometimes a defective matrix and not diagonalizable. In this situation, the critical energy value W_{tot}^* must be treated in a lower-dimensional subspace or manifold [69], which is offered by the condition specified as

$$W_{tot}^* = \arg \min_{y \in \mathbb{y}} W_{tot}(\mathbf{R}), \tag{2}$$

subject to $\{\mathbb{y}|\partial x W_{tot} = 0, \partial_x^2 W_{tot} < 0\}$. Herein, the condition describes the total PE at a certain point $\mathbf{R}^* = (x^*, y^*)$ that simultaneously satisfies both a peak of the energy ridge in the subspace that the x-components of W_{tot} are mapped into and a local minimum in the subspace ($\mathbb{y}$) of the y-component of W_{tot}. Consequently, the critical energy value W_{tot}^*, shown in Fig. 2 (red dashed lines), is expressed as a function of J_e, independently of $\mathbf{R}$: $W_{tot}^*(J_e) = W_{tot}(\mathbf{R}^*(J_e), J_e)$. The skyrmion at $\mathbf{R}_0 = (-274, 0)$ nm and $J_e = +30$ MA/cm² has the *off* state $W_{tot}(\mathbf{R}_0, J_e) < W_{tot}^*(J_e)$ in Fig. 2(a), indicating that the initial energy does not exceed the energy barrier. The skyrmion at $\mathbf{R}_0 = (-274, 0)$ nm and $J_e = +50$ MA/cm² can likewise be interpreted as the *on* state due to $W_{tot}(\mathbf{R}_0, J_e) > W_{tot}^*(J_e)$, indicating that the initial energy overcomes the energy barrier. In contrast, the initial energy $W_{tot}(\mathbf{R}_0, J_e)$ with $\mathbf{R}_0 = (+274, 0)$ nm in the reverse direction is not sufficient to overcome the energy barrier $W_{tot}^*(J_e)$ in the range $-116 \leq J_e$ (MA/cm²) < 0, and thus the *off* state is maintained. As a result, skyrmions driven in different directions experience significantly different *on/off* transmission at the pinning site.

Next, to better understand the origin of the asymmetric transmission, we investigate the

symmetry of PEs in the forward ($J_e > 0$) and reverse ($J_e < 0$) directions. Figure 3 shows a large

difference in the critical energy value (indicated by red horizontal dotted lines) of total PE between

the forward and reverse directions, as clearly seen in the bottom panel of Fig. 3. To describe the

symmetry of the total PE, we decompose it into the sum of the J_e-dependent part $W_{STT}(\mathbf{R}, J_e)$

and J_e-independent part $W_{con}(\mathbf{R})$ [70], as shown in the middle and top panels of Fig. 3,

respectively. Here, the J_e-dependent STT-PE W_{STT} is oddly symmetric with respect to both

inversions of $J_e \rightarrow -J_e$ and $\mathbf{R} \rightarrow -\mathbf{R}$. However, the location of critical points $\mathbf{R}^*$ is not oddly

symmetric with respect to the inversion of $J_e \rightarrow -J_e$, as indicated by red vertical dotted lines in

Fig. 3. This discrepancy in symmetry between W_{STT} and $\mathbf{R}^*$ induces significant difference

between forward and reverse directions; the results summarized in the middle panels of Fig. 3

clearly show that W_{STT} at $\mathbf{R}^*$ increases in the forward direction and decreases in the reverse

direction as indicated by the blue arrows. For a control experiment, we examine the symmetric

case to be $\mathbf{R}^* \rightarrow -\mathbf{R}^*$ with respect to the inversion of $J_e \rightarrow -J_e$, i.e., the pinning sites are

patterned on both top and bottom sides. In this case, we confirm that W_{STT} at $\mathbf{R}^*$ identically

decreases in the forward and reverse directions as shown in Fig. S2 [71]. In summary, the

asymmetrical distribution of the pinning site on two sides breaks the symmetry of W_{STT} at $\mathbf{R}^*$

in transverse directions (along the y-axis), which results in the asymmetric transmission of

longitudinal motions in the forward and reverse directions (along the x-axis).

To distinguish the characteristic dynamics for *on/off* transmission, we estimate the

average skyrmion velocity as $\bar{v} = [x(T) - x(0)]/T$, where T is the elapsed time when the

initial skyrmion arrives at a destination on the opposite side $x(T) = -x(0)$. Therefore, the

average velocity in the off state is $\bar{v} = 0$ due to the infinite time $T \to \infty$ it takes to arrive at the

destination, whereas the average velocity in the on state shows a nonzero value as a function of

J_e. Figure 4(a) shows the results of the numerical simulations in which $\bar{v}$ varies asymmetrically

as a function of J_e, similarly to the I–V characteristic curve of an electrical diode. We now define

the threshold current density J_{th} as the minimum current density required for the skyrmion to

pass through the pinning site. As an analog of electrical diodes, it is noteworthy that skyrmions

driven in different directions require significantly different J_{th} from the numerical results in Fig.

4(a): $J_{th} = 43.5 \pm 3.0$ MA/cm^2 and $J_{th} = -123.5 \pm 7.50$ MA/cm^2 for the forward and reverse

directions of skyrmion motion, respectively. In addition, we propose that the initial position can

be a system parameter to modify the threshold current density. In the nondissipative model ($\alpha =$

0), the exact solution for the system parameter variable $\mathbf{R}_0 = (x_0, 0)$ can be calculated from the

given J_{th} that satisfies $W_{tot}(\mathbf{R}_0, J_{th}) = W_{tot}^*(J_{th})$. The results of x_0 versus J_{th} in the

forward/reverse directions are plotted in Fig. 4(b), which are in good agreement with the

micromagnetic simulation results (circle symbols) in the limit of small dissipation coefficient α.

The threshold current density of the simulations is required to be slightly higher than that of the

models, due to energy dissipation from the damping parameter ($\alpha = 0.01$) of the simulations.

Finally, we discuss the comparison of the physical interpretation of this result with those of other transport phenomena. Information transport of conserved physical quantities in various diode structures can be described in terms of linear models relating fluxes and potentials, e.g., Ohm's law for current flux–potential, the Hagen–Poiseuille law or Darcy's law for fluid flux–pressure, or the Fourier law for heat flux–temperature. In the case of skyrmion transport carrying the conserved quantity Q, the skyrmionic analogs of flux and potential are the transport rate of the skyrmion number $\dot{Q}$ and PE W, respectively. Likewise, the flux density is qv, with the volumetric density of skyrmion number q and the drift velocity of skyrmion transport v. The linear model of skyrmionic flux–potential, based on the steady-state Boltzmann transport theory for an isolated single skyrmion ignoring inter-skyrmion interactions and nonequilibrium diffusion, can be described in the form of the Thiele equation $\mathbf{G} \times v + \widehat{D}v = \hat{\rho}qv = -\nabla W$ [41] with resistivity tensor ρ for skyrmion transport. Here, the first term (gyroforce) results in the Hall-like response ($\rho_\perp$) that the skyrmion intrinsically exhibits transverse motion [35,36] without rotational motion or external magnetic field. Hence, the skyrmion transport is different from that of electrons and fluids, the transverse motions of which extrinsically occur under the conditions for the Lorentz force and the Magnus force, respectively.

From this standpoint, we implement asymmetric *on/off* transmissions in a diode structure employing magnetic skyrmions as information carriers. The key element of the skyrmion diode implementation is to seek geometric symmetry breaking by asymmetrically distributing the

pinning sites on the two sides of the nanostrip so that the symmetry of mirror reflection is broken in the transverse direction (y-axis) and obeyed in the longitudinal direction (x-axis) of the driving current. Consequently, the transverse symmetry of the location of the critical point (topographic saddle point) is broken in the PE barrier, which derives unidirectional motion in the longitudinal directions. Here, the time-reversal symmetry is not considered because the equation of skyrmion motion is not inherently time-reversal-invariant, unlike the Maxwell equations and Newton's equations of motion. In our model, we extend the effective PE for driving forces to various forms such as spin-Hall torque [72–75], Rashba torque [74–76], and voltage-controlled magnetic anisotropy [77,78], in addition to the STT-PE employed here. Based on the equipotential line with the effective driving PE and the topography of PE, our approach can be time-efficiently used as a basis to design skyrmion-based logic devices such as diode elements, transistors, logic gates, and other cascaded devices for more complex arithmetic operations.

References

* Author to whom all correspondence should be addressed: kisuk@unist.ac.kr

[1] K. H. Randy and B. Gaetano, *Contemporary Logic Design* (Pearson Prentice Hall, 2005).

[2] A. Kitai, *Principles of Solar Cells, LEDs and Diodes: The Role of the PN Junction* (John Wiley & Sons, Chichester, 2011).

[3] X. Huo and G. Yossifon, Phys. Rev. Lett. **123**, 194502 (2019).

[4] J. Li, X. Zhou, J. Li, L. Che, J. Yao, G. McHale, M. K. Chaudhury, and Z. Wang, Sci. Adv. **3**, eaao3530 (2017).

[5] J. Rousselet, L. Salome, A. Ajdari, and J. Prostt, Nature **370**, 446-447 (1994).

[6] P. C. Sousa, F. T. Pinho, M. S. N. Oliveira, and M. A. Alves, J. Non-Newtonian Fluid Mech. **165**, 652-671 (2010).

[7] C.W. Chang, D. Okawa, A. Majumdar, and A. Zttl, Science **314**, 1121 (2006).

[8] B. Li, L. Wang, and G. Casati, Phys. Rev. Lett. **93**, 184301 (2004).

[9] A. E. Serebryannikov, Phys. Rev. B **80**, 155117 (2009).

[10] A. E. Serebryannikov and E. Ozbay, Opt. Express **17**, 13335 (2009).

[11] X.-F. Li, X. Ni, L. Feng, M.-H Lu, C. He, and Y.-F. Chen, Phys. Rev. Lett. **106**, 084301 (2011).

[12] B. Liang, X. S. Guo, J. Tu, D. Zhang, and J. C. Cheng, Nat. Mater. **9**, 989 (2010).

[13] M. D. Tocci, M. J. Bloemer, M. Scalora, J. P. Dowling, and C. M. Bowden, Appl. Phys. Lett. **66**, 2324 (1995).

[14] D.-W. Wang, H.-T. Zhou, M.-J. Guo, J.-X. Zhang, J. Evers, and S.-Y. Zhu, Phys. Rev. Lett. **110**, 093901 (2013).

[15] J. Lan, W. Yu, R. Wu, and J. Xiao, Phys. Rev. X **5**, 041049 (2015).

[16] X. Xing, P. W. Pong, and Y. Zhou, J. Appl. Phys. **120**, 203903 (2016).

[17] J. Wang, J. Xia, X. Zhang, X. Zheng, C. Li, L. Chen, Y. Zhou, J. Wu, H. Yin, R. Chantrell, and Y. Xu, Appl. Phys. Lett. **117**, 202401 (2020).

[18] L. Zhao, X. Liang, J. Xia, G. Zhao, and Y. Zhou, Nanoscale **12**, 9507 (2020).

[19] M. Remoissenet and J. A. Whitehead, Am. J. Phys. **63**, 381 (1995).

[20] L. Khaykovich, Science **296**, 1290 (2002).

[21] T. Herr, V. Brasch, J. D. Jost, C. Y. Wang, N. M. Kondratiev, M. L. Gorodetsky, and T. J. Kippenberg, Nat. Photonics **8**, 145 (2014).

[22] A. Komarov, K. Komarov, A. Niang, and F. Scanchez, Phys. Rev. A **89**, 013833 (2014).

[23] A. Fert, V. Cros, and J. Sampaio, Nat. Nanotech. **8**, 152 (2013).

[24] F. Jonietz, S. Mühlbauer, C. Pfeiderer, A. Neubauer, W. Münzer, A. Bauer, T. Adams, R. Georgi, P. Böni, R. A. Duine, K. Everschor, M. Garst, and A. Rosch, Sience **330**, 1648 (2010).

[25] J. Iwasaki, M. Mochizuki, and N. Nagaosa, Nat. Nanotechnol. **8**, 742 (2013).

[26] J. Sampaio, V. Cros, S. Rohart, A. Thiaville, and A. Fert, Nat. Nanotechnol. **8**, 839 (2013).

[27] T. Schulz, R. Ritz, A. Bauer, M. Halder, M. Wagner, C. Franz, C. Pfleiderer, K. Everschor, M. Garst, and A. Rosch, Nat. Phys. **8**, 301-304 (2012).

[28] J. Iwasaki, W. Koshibae, and N. Nagaosa, Nano Lett. **14**, 4432 (2014).

[29] S. Woo, K. M. Song, H.-S. Han, M.-S. Jung, M.-Y. Im, K.-S. Lee, K. S. Song, P. Fischer, J.-I. Hong, J. W. Choi, B.-C. Min, H. C. Koo, and J. Chang, Nat. Commun. **8**, 15573 (2017).

[30] N. Nagaosa and Y. Tokura, Nat. Nanotechnol. **8**, 899 (2013).

[31] M. Raju, A. Yagil, A. Soumyanarayanan, A. K. Tan, A. Almoalem, F. Ma, O. M. Auslaender, and C. Panagopoulos, Nat. Commun. **10**, 696 (2019).

[32] T. H. R. Skyrme, Nucl. Phys. **31**, 556–569 (1962).

[33] I. Dzyaloshinskii, J. Phys. Chem. Solids **4**, 241 (1958).

[34] T. Moriya, Phys. Rev. **120**, 91 (1960).

[35] W. Jiang, X. Zhang, G. Yu, W. Zhang, X. Wang, M. B. Jungfleisch, J. E. Pearson, X. Cheng, O. Heinonen, K. L. Wang *et al.*, Nat. Phys. **13**, 162 (2017).

[36] K. Litzius, I. Lemesh, B. Krüger, P. Bassirian, L. Caretta, K. Richter, F. Büttner, K. Sato, O. A. Tretiakov, J. Förster *et al.*, Nat. Phys. **13**, 170 (2017).

[37] J. Müller and A. Rosch, Phys. Rev. B **91**, 0544110 (2015).

[38] C. Hanneken, A. Kubetzka, K. Von Bergmann, and R. Wiesendanger, New J. Phys. **18**, 055009 (2016).

[39] D. Stosic, T. B. Teresa, and M. V. Milošević, Phys. Rev. B **96**, 214403 (2017).

[40] J. Castell-Queralt, L. González-Gómez, N. Del-Valle, and C. Navau, Phys. Rev. B **101**, 140404(R) (2020).

[41] A. A. Thiele, Phys. Rev. Lett. **30**, 230 (1973).

[42] See Supplemental Material, which includes Refs. [43-50], for the detailed simulation method and material parameters.

[43] See http://math.nist.gov/oommf.

[44] L. D. Landau and E. M. Lifshitz, Phys. Z. Sowjet. **8**, 153 (1935).

[45] T. L. Gilbert, Phys. Rev. **100**, 1243 (1955).

[46] J. C. Slonczewski, J. Magn. Magn. Mater. **159**, L1 (1996)

[47] L. Berger, Phys. Rev. B **54**, 9353 (1996).

[48] A. Vansteenkiste, J. Leliaert, M. Dvornik, M. Helsen, F. Garcia-Sanchez, and B. Van Waeyenberge, AIP Adv. **4**, 107133 (2014).

[49] X. Zhang, Y. Zhou, and M. Ezawa, Phys. Rev. B **93**, 024415 (2016).

[50] F. Garcia-Sanchez, J. Sampaio, N. Reyren, V. Cros, and J.-V. Kim, New J. Phys. **18**, 075011 (2016).

[51] X. C. Zhang, G. P. Zhao, H. Fangohr, J. P. Liu, W. X. Xia, J. Xia, and F. J. Morvan, Sci. Rep. **5**, 7643 (2014).

[52] Y. Tchoe and J. H. Han, Phys. Rev. B **85**, 174416 (2012).

[53] S. Lee, H.-S. Han, D.-H. Jung, N. Kim, M. Kang, H.-J. Ok, and K.-S. Lee, J. Magn. 25, 458-462 (2020).

[54] S.-G. Je, D. Thian, X. Chen, L. Huang, D.-H. Jung, W. Chao, K.-S. Lee, J.-I. Hong, A.

Soumyanarayanan, and M.-Y. Im, Nano Lett. 21, 1253 (2021).

[55] S. Rohart and A. Thiaville, Phys. Rev. B **88**, 184422 (2013).

[56] F. Garcia-Sanchez, P. Borys, A. Vansteenkiste, J.-V. Kim, and R. L. Stamps, Phys. Rev. B **89**, 224408 (2014).

[57] M.-W. Yoo, V. Cros, and J.-V. Kim, Phys. Rev. B **95**, 184423 (2017).

[58] L. Desplat, J.-V. Kim, and R. L. Stamps, Phys. Rev. B **99**, 174409 (2019).

[59] K. Everschor, M. Garst, R. A. Duine, and A. Rosch, Phys. Rev. B **84**, 064401 (2011).

[60] I. Makhfudz I, B. Krüger, and O. Tchernyshyov, Phys. Rev. Lett. **109**, 217201 (2012).

[61] J.-V. Kim, Solid State Phys. **63**, 217 (2012).

[62] A. V. Khvalkovsiy, J. Grollier, A. Dussaux, Konstantin A. Zvezdin, and V. Cros, Phys. Rev. B **80**, 140401 (2009).

[63] G. Consolo, C. Currò, and G. Valenti, Appl. Math. Comput. **217**, 8204 (2011).

[64] G. Bertotti, C. Serpico, and I. D. Mayergoyz, Phys. Rev. B **90**, 104430 (2014).

[65] S. Salahuddin, D. Datta, and S. Datta, "Spin Transfer Torque as a Non-Conservative Pseudo-Field" (2008), arXiv:0811.3472.

[66] G. Henkelman and H. Jónsson, J. Chem. Phys. **111**, 7010 (1999).

[67] M. P. Gutiérrez, C. Argáez, and H. Jónsson, J. Chem. Theory Comput. **13**, 125 (2017).

[68] G. P. Müller, P. F. Bessarab, S. M. Vlasov, F. Lux, N. S. Kiselev, S. Blügel, V. M. Uzdin, and H. Jónsson, Phys. Rev. Lett. **121**, 197202 (2018).

[69] For simplification of numerical calculation, we deal with the class of differentiable manifolds in the n-dimensional Euclidean space, aside from Riemannian manifolds.

[70] It was reported that W_{con} is independent of the spin-torque parameters β and J_{e} in the reference [57].

[71] Further discussion on the symmetry of PEs and quantitative examination is given in the Supplemental Material [42].

[72] M. Dyakonov and V. Perel, JETP Lett. **13**, 467 (1971).

[73] J. E. Hirsch, Phys. Rev. Lett. **83**, 1834 (1999).

[74] E. Martinez, S. Emori, and G. S. Beach, Appl. Phys. Lett. **103**, 072406 (2013).

[75] B. S. Kim, J. Phys. Condens. Matter. **3**1, 383001 (2019).

[76] Yu. A. Bychkov and E. I. Rashba, JETP Lett. **39**, 78 (1984).

[77] P. Upadhyaya, G. Yu, P. K. Amiri, and K. L. Wang, Phys. Rev. B **92**, 134411 (2015).

[78] R. Verba, V. Tiberkevich, I. Krivorotov, and A. Slavin, Phys. Rev. Appl. **1**, 044006 (2014).

Figure captions

FIG. 1. (Color online) Schematic illustration of model system. (a) Geometry of the model, surface of the confining PE, and 2D pseudo-color plot of the confining PE. The arrows indicate the magnetization configuration of the single skyrmion, and its colors represent the out-of-plane component (red = up, blue = down) of the magnetization. In the pseudo-color plot, the black color indicates the area where the skyrmion is not allowed to stably exist. The trajectories of the skyrmion motion calculated from micromagnetic simulations under the current density $J_e = 5$ MA/cm^2 for the direction of (b) forward and (c) reverse, respectively.

FIG. 2. (Color online) Schematic view (x-W plane) of the total PE surface for the given current densities (+30, +50 and –5 MA/cm^2) as noted. The colors are made to be somewhat transparent to reveal that the energy surfaces are tilted. The small circles (green) indicate the initial state $[\mathbf{R}_0, W_{\text{tot}}(\mathbf{R}_0)]$. The dashed lines indicate equipotential lines correspond to the initial energy (black) and the critical energy value W_{tot}^* (red), respectively.

FIG. 3. (Color online) Profiles of W_{con}, W_{STT}, and $W_{\text{con}} + W_{\text{STT}}$ on the selected x-positions for x_0 (black solid line), x^* (red solid line), and $-x_0$ (orange solid line) as respectively marked in the first row, for the forward and reverse directions with the given the given current density $J_e = 5$ MA/cm^2. The small circles (green) indicate the initial states for each case. The red dotted lines

indicate the critical state composed of y^* (vertical) and W_{tot}^* (horizontal). The horizontal black dotted line indicates the initial energy level of total PE, $W_{\text{tot}}(\mathbf{R}_0)$. If $W_{\text{tot}}^* > W_{\text{tot}}(\mathbf{R}_0)$, the gap between W_{tot}^* and $W_{\text{tot}}(\mathbf{R}_0)$ is indicated by filling in grey, which means that the skyrmion is forbidden to overcome the energy barrier (W_{tot}^*) from the initial state ($W_{\text{tot}}(\mathbf{R}_0)$). If $W_{\text{tot}}^* < W_{\text{tot}}(\mathbf{R}_0)$, the possible equipotential path to overcome the energy barrier is indicated by the blue arrows.

FIG. 4. (Color online) Diode characteristics curves for the asymmetry of *on/off* transmission. (a) Average velocity $\bar{v}$ as a function of the current density J_e, calculated from micromagnetic simulations. (b) Numerical calculations of the analytical equations (solid lines) for the threshold current density J_{th} as a function of the initial *x*-position x_0, compared to micromagnetic simulations (open circles), for the forward (black) and reverse (red) directions, as noted.
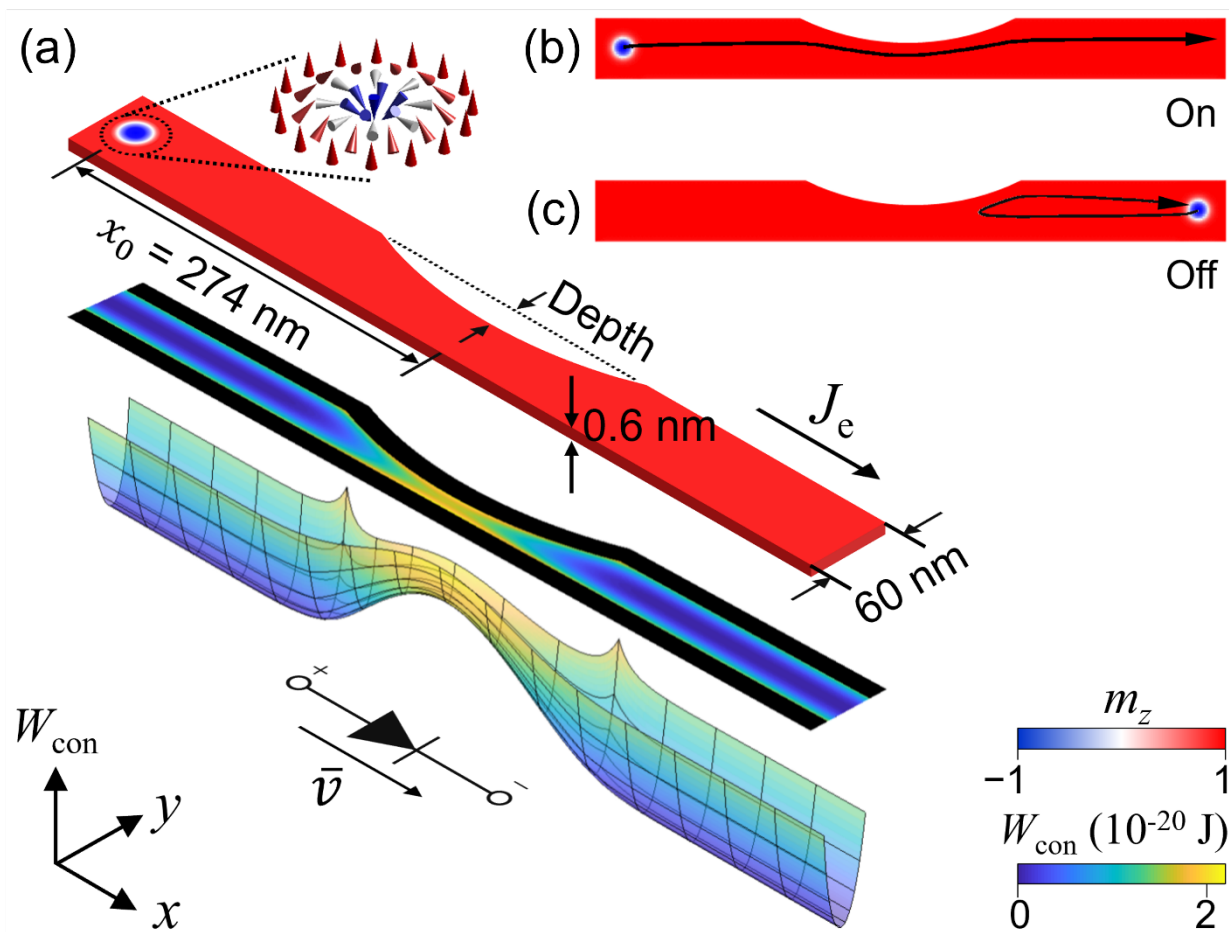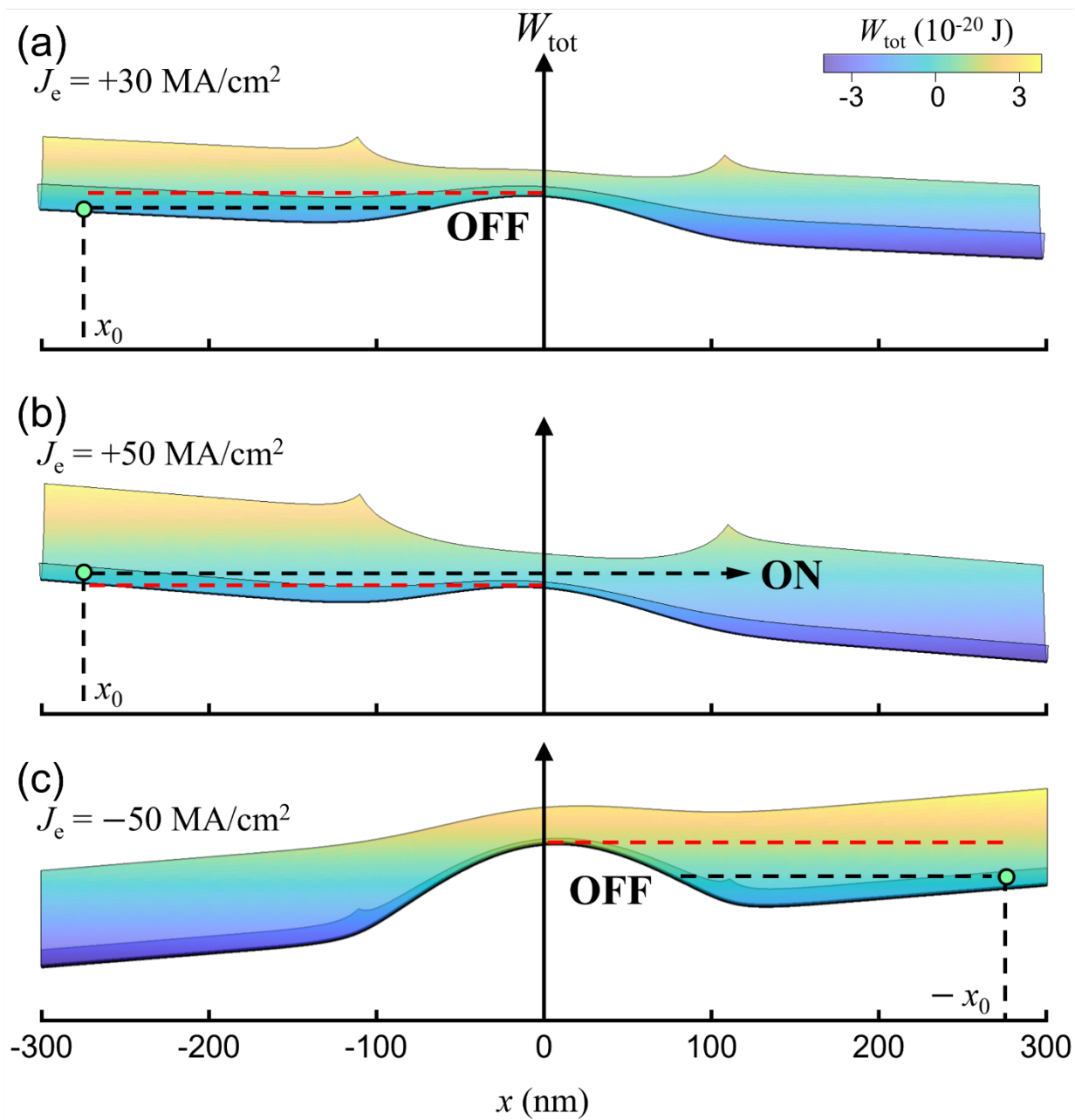
FIG. 1.

(a)

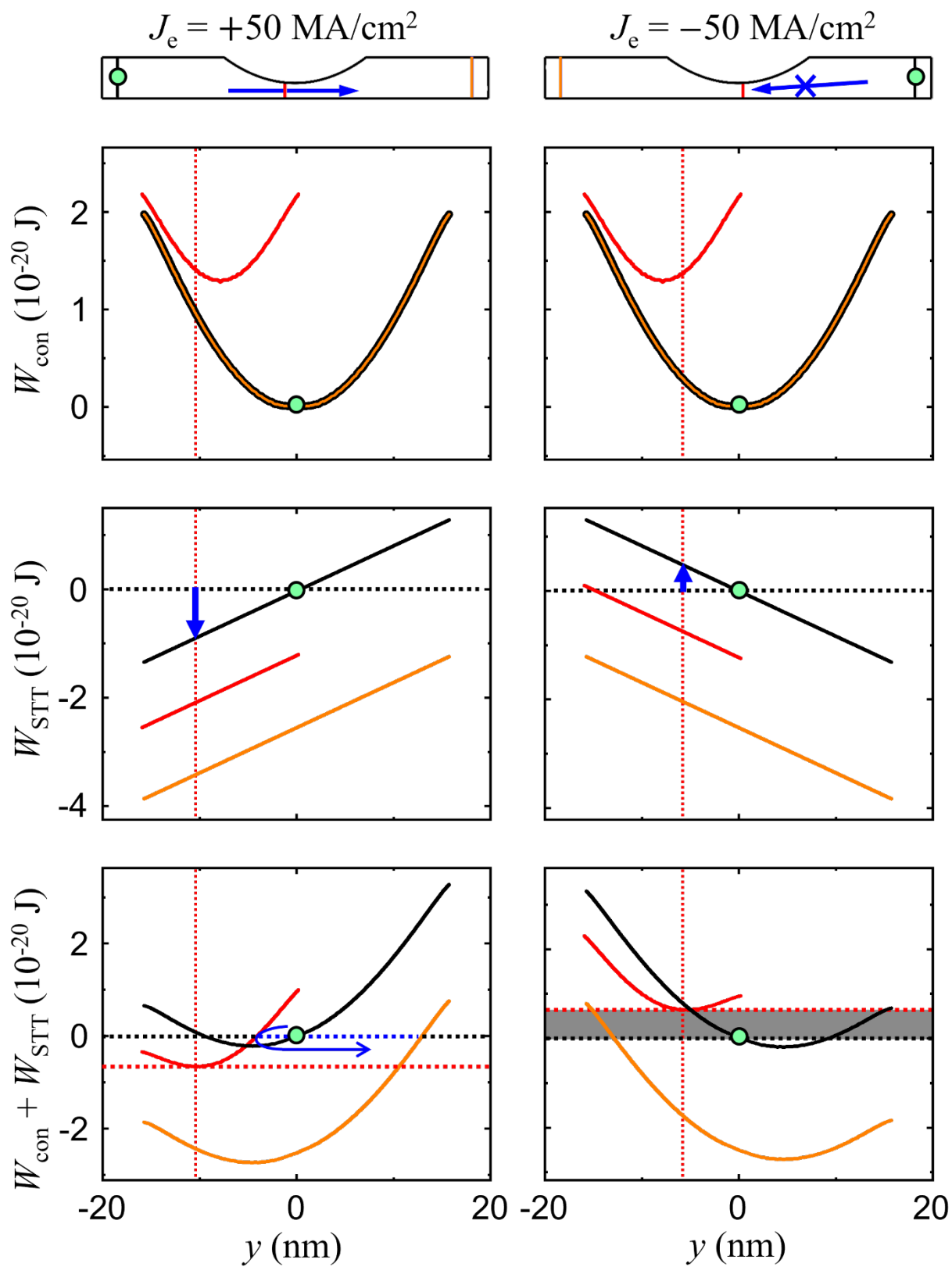$x_0 = 274$ nm

Depth

0.6 nm

J_e

60 nm

W_{con}

y

x

$\bar{v}$

(b)

On

(c)

Off

m_z

−1   1

W_{con} (10⁻²⁰ J)

0   2

FIG. 2.

FIG. 3.

FIG. 4.